

# Electron-Transport Layers Employing Strongly Bound Ligands Enhance Stability in Colloidal Quantum Dot Infrared Photodetectors

Yangning Zhang, Maral Vafaie, Jian Xu, Joao M. Pina, Pan Xia, Amin M. Najarian, Ozan Atan, Muhammad Imran, Ke Xie, Sjoerd Hoogland, and Edward H. Sargent\*

**Solution-processed photodetectors based on colloidal quantum dots (CQDs) are promising candidates for short-wavelength infrared light sensing applications. Present-day CQD photodetectors employ a CQD active layer sandwiched between carrier-transport layers in which the electron-transport layer (ETL) is composed of metal oxides. Herein, a new class of ETLs is developed using n-type CQDs, finding that these benefit from quantum-size effect tuning of the band energies, as well as from surface ligand engineering. Photodetectors operating at 1450 nm are demonstrated using CQDs with tailored functionalities for each of the transport layers and the active layer. By optimizing the band alignment between the ETL and the active layer, CQD photodetectors that combine a low dark current of  $\approx 1 \times 10^{-3}$  mA cm<sup>-2</sup> with a high external quantum efficiency of  $\approx 66\%$  at 1 V are reported, outperforming prior reports of CQD photodetectors operating at  $>1400$  nm that rely on metal oxides as ETLs. It is shown that stable CQD photodetectors rely on well-passivated CQDs: for ETL CQDs, a strongly bound organic ligand *trans*-4-(trifluoromethyl)cinnamic acid (TFCA) provides improved passivation compared to the weakly bound inorganic ligand tetrabutylammonium iodide (TBAI). TFCA suppresses bias-induced ion migration inside the ETL and improves the operating stability of photodetectors by 50× compared to TBAI.**

## 1. Introduction

Short-wavelength infrared (SWIR) photodetectors are needed in medical imaging, machine vision, and biometric authentication.<sup>[1]</sup> In autonomous driving, SWIR detectors with peak sensitivities in the range 1400–1500 nm distinguish water from ice based on their distinct absorption features and can be used to detect winter road conditions.<sup>[2,3]</sup>

Solution-processed photodetectors such as those based on colloidal quantum dots (CQDs) enable integration with a variety of substrates, including silicon-based read-out integrated

circuits.<sup>[4–7]</sup> PbS CQDs are well-suited to SWIR photodetection in light of their size-tuned bandgap and strong absorption in the IR region. The latest CQD photodetectors have adopted the photodiode architecture consisting of a CQD-based active layer, a CQD-based hole-transport layer (HTL), and a metal oxide-based electron-transport layer (ETL).<sup>[7–10]</sup>


High-efficiency photodetectors require accurate control of the optoelectronic properties of each layer. To reach a peak sensitivity in the wavelength range of 1400–1500 nm, small bandgap PbS CQDs are used as active layers, and their relatively deep conduction band position limits the selection of ETs. Known metal oxides such as ZnO or TiO<sub>2</sub> do not offer the combination of properties needed for SWIR CQD detectors: the requisite union of band alignment at the interface, and stable performance at the operating wavelengths.<sup>[8,10]</sup>

CQD-based transport layers benefit from tunable optoelectronic properties through surface ligand engineering and quantum-size effect tuning. While CQD

HTLs have been extensively studied and improved, CQD ETLs are rarely explored.<sup>[11–13]</sup> Here we develop n-type CQDs as ETLs and tailor their band-edge positions for efficient charge extraction at the active layer/ETL interface. We fabricate all-CQD photodetectors in which CQDs of the same composition but with different sizes and ligand passivation were used to produce functionalities optimized separately for the active layer and charge-transport layers. The CQD photodetectors operating at 1450 nm exhibit a high external quantum efficiency (EQE) of 66% and a low dark current of  $\approx 1 \times 10^{-3}$  mA cm<sup>-2</sup> at 1 V, which has not been realized simultaneously in the prior works that used metal oxides as ETLs.

We find that the surface passivation of CQDs is crucial to suppressing ion migration and preventing performance degradation in CQD photodetectors. Therefore, we develop a strategy to improve the passivation of ETL CQDs using strongly bound organic ligands. Specifically, we demonstrate that ETLs employing a strong organic ligand *trans*-4-(trifluoromethyl)cinnamic acid (TFCA) improve the dark current stability of CQD photodetectors by 50× compared to ETLs employing a weakly bound inorganic ligand tetrabutylammonium iodide (TBAI).

Y. Zhang, M. Vafaie, J. Xu, J. M. Pina, P. Xia, A. M. Najarian, O. Atan, M. Imran, K. Xie, S. Hoogland, E. H. Sargent  
Department of Electrical and Computer Engineering  
University of Toronto  
10 King's College Road, Toronto, Ontario M5S 3G4, Canada  
E-mail: ted.sargent@utoronto.ca

 The ORCID identification number(s) for the author(s) of this article can be found under <https://doi.org/10.1002/adma.202206884>.

DOI: 10.1002/adma.202206884

## 2. Results and Discussion

To achieve efficient charge transport in CQD solids for device applications, it is necessary to replace long insulating oleic acid ligands originally attached to the CQDs from synthesis with shorter conductive ligands. These ligands also modulate the energy levels of CQDs. Surface modification together with quantum-size effect tuning enables us to engineer the electronic properties of CQDs.

To fabricate the CQD ETLs, we select two different n-type ligands, TBAI as a representative inorganic atomic ligand, and TFCA as an organic ligand (see **Figure 1a** for their chemical structures). We used TBAI—known to result in n-type behavior of CQD solids and increase their conductivity,<sup>[14–16]</sup> and recently used in photodetectors<sup>[17]</sup>—as control; these provided a basis of comparison with the new class of ETLs developed herein based on the organic carboxylate TFCA. Both classes of ligand contain halide: in the case of TBAI, the iodine atoms attach directly to the CQD surface; while the fluorine atoms in TFCA do not (Figure 1c).<sup>[18,19]</sup>

We carried out density functional theory (DFT) calculations to investigate the binding strength of TBAI and TFCA to CQDs. The dominant facets PbS (100) and PbS (111) were selected for

binding energy ( $E_b$ ) calculations.<sup>[20,21]</sup> We find that the hollow site is the most stable adsorption configuration of both ligands on PbS surfaces (Figure S1, Supporting Information). The differential charge densities (Figure 1b) show that  $I^-$  and  $TFCA^-$  as adsorbates attract electrons from neighboring Pb atoms. The  $E_b$  of  $I^-$  to CQD surface are relatively small,  $-1.23$  and  $-1.55$  eV for (100) and (111) facets. For TFCA, deprotonated  $TFCA^-$  binds to the CQD surface through the carboxylic group with  $E_b$  of  $-3.39$  and  $-4.19$  eV to (100) and (111) facets. The larger binding strength of TFCA than TBAI is connected with the stronger electronegativity of O than I, and the electron-withdrawing fluorinated functional group. The studies indicate that TFCA may be less prone to detach from CQD surfaces than TBAI.

Next, we carried out ligand exchanges on CQDs. TFCA involves a solution-phase exchange, while TBAI employs a solid-state exchange.<sup>[14,19]</sup> Solution-phase exchange usually creates more homogeneous CQD films than solid-state exchange, and also provides better control of removing the organic residues. Fourier-transform infrared (FTIR) spectroscopy and X-ray photoelectron spectroscopy (XPS) showed that the native oleic acid was removed, and gave evidence that TFCA became attached to the CQDs (Figures S2 and S3, Supporting Information). We compared the transport properties of TFCA- and TBAI-exchanged CQD solids using space-charge-limited current (SCLC) measurements, and found that the electron mobility of TFCA-CQDs was lower than TBAI-CQDs (Figure S4 and Table S1, Supporting Information), consistent with the larger steric hindrance from TFCA. To use the TFCA-CQDs as ETL, we need to decrease the thickness of this layer to overcome transport limitations.

To investigate the charge carrier dynamics in ligand exchanged CQD films, we performed ultrafast transient absorption (TA) measurements (see Figure S5, Supporting Information for the kinetic traces of the band-edge bleaching in different CQDs and Table S2, Supporting Information for biexponential decay fitting results). SCLC and TA can both be used to investigate the traps in CQDs. TA is capable of characterizing the CQD film alone; while SCLC is measured on electron-only devices (with ITO/ZnO/CQD/LiF/Ag structure), and it can be influenced by additional layers such as ZnO and LiF proximate the CQD layer. The faster decay of TBAI-CQDs than TFCA-CQDs observed in TA implies faster charge trapping in TBAI-CQDs, which originates from inadequate passivation of surface defects. Under-charged (i.e., reduced) Pb atoms on the surface of CQDs are believed to be responsible for the sub-bandgap states.<sup>[18]</sup> The relatively small binding energy of TBAI to CQDs (Figure 1b) suggests that it binds weakly to Pb atoms and fails to provide complete surface passivation.

To integrate the n-type CQD ETLs into a photodiode, we sought to match the energy levels of each layer for band alignment. Larger CQDs (with an excitonic peak at 1450 nm) passivated with mixed lead halides were used as the active layer. The mixed halide exchange strategy was adopted here because it has been reported to produce well-passivated CQDs with improved charge-transport properties.<sup>[22]</sup> XPS shows that three kinds of halides (I, Br, and Cl) are present in the mixed halide-exchanged CQD film (Figure S6, Supporting Information). For both the ETL and the HTL, smaller CQDs (with an excitonic peak at 950 nm) were used, but they were

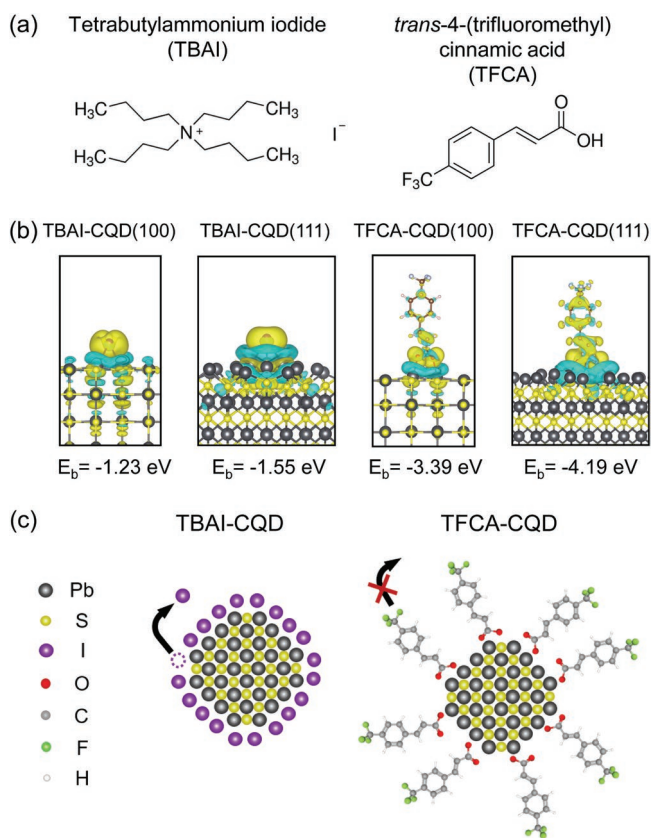


**Figure 1.** Chemical structures of n-type ligands and their binding strengths to CQD surfaces. a) Chemical structures of TBAI and TFCA. b) Differential charge densities of  $I^-$  and  $TFCA^-$  on the PbS (100) and (111) facets. Pb and S atoms are represented by grey and yellow spheres. The yellow or blue areas represent a gain or loss of electrons. Binding energies ( $E_b$ ) are listed below. c) Schematic of bound ligands detaching from CQD surface.

exchanged with different ligands: TBAI or TFCA for the ETL, and 1,2-ethanedithiol (EDT) for the HTL. We confirmed the average sizes of the smaller CQDs and the larger CQDs to be 2.9 and 5.0 nm using transmission electron microscopy (TEM, see Figures S7 and S8, Supporting Information). The energy levels of each layer were determined from UV photoelectron spectroscopy (UPS) and UV-visible absorption measurements, as summarized in **Figure 2a**. The conduction band (CB) and valence band (VB) positions of TFCA are both 0.3 eV deeper than TBAI, consistent with reported values.<sup>[19,23]</sup> The energy level shift was believed to be proportional to the effective surface dipole, which is a sum of the intrinsic dipole of the free ligand and the induced dipole at the ligand/CQD interface. The fluorinated ligands tend to shift the band-edges of CQDs toward deeper energy levels than non-fluorinated ligands.<sup>[19]</sup>

In order to maintain the integrity of all the CQD layers during the photodetector fabrication, it is important to take into consideration the process compatibility and orthogonality between each layer.<sup>[11]</sup> The choice of solvent and the sequence of deposition are key factors. We found that an inverted (p-i-n) structure in which the HTL is below the active layer and the ETL is on top ensures compatibility between CQD layers (**Figure 2b**): the solvents of upper layers are orthogonal to the underlying layers. In contrast, the standard (n-i-p) structure is not compatible, because the deposition of active layer CQDs easily dissolves the underlying ETL of TFCA-CQDs. For a fair comparison, we also adopted the process-compatible inverted structure for our control photodetectors employing TBAI-CQDs as the ETL.

We optimized the thickness of TFCA ETL, finding that 10 nm produces the best combination of low dark current and high EQE (**Figure S9**, Supporting Information). The optimized device performance using TFCA-CQDs or TBAI-CQDs as the ETL was compared. The current density–voltage curves measured in the dark are shown in **Figure 2c**. At 1 V reverse bias, TFCA and TBAI devices have similar dark current densities of  $\approx 1 \times 10^{-3}$  mA cm<sup>-2</sup>. The EQE at 1450 nm of both devices shows a bias-dependent behavior, increasing from  $\approx 37\%$  at 0 V to  $\approx 66\%$  at 1 V (**Figure 2d**). The EQEs of TFCA devices are slightly higher than those of TBAI devices at 0.3 V and 0.5 V. Compared to reported photodetectors at similar wavelengths, the TFCA devices achieved the best combination of EQE and low dark current (**Figure 2e**). This we attribute to the better band alignment at the active layer/ETL interface in our photodetectors (see band diagrams in **Figure 2a**).

The energy level alignment of ETLs with respect to the active layer determines electron extraction capability. We used modeling to understand the impact of energy level alignment on device performance (**Figure S10**, Supporting Information). When the electron affinity (EA) of the ETL (as in the case of metal oxides) is smaller than that of the active layer, the dark current and the EQE are not optimal. When the EAs of ETL and active layer are well-aligned (as in the cases of TFCA and TBAI devices), the dark current and the EQE are optimal and remain unchanged when we further vary the EA. This is consistent with our experimental results showing that the performance of TFCA and TBAI devices are similar, and both are superior to reported metal oxides.

We then quantified the photodetection characteristics of the resultant CQD photodetectors. At 1450 nm, there was no

obvious difference in the responsivities and detectivities of TFCA and TBAI devices, each reaching a maximum responsivity of  $\approx 0.4$  A W<sup>-1</sup>, and a maximum detectivity of  $3 \times 10^{10}$  cm Hz<sup>0.5</sup> W<sup>-1</sup> (**Figure 3a,b**). The noise spectra of TFCA and TBAI devices are provided in **Figure S11**, Supporting Information. The photodetection speed was determined by measuring the transient photocurrent responses, and the fall time corresponds to the time interval between 10% and 90% of the maximum photocurrent. As shown in **Figure 3c**, the fall time of TFCA devices decreases with increasing bias, and the minimum fall time is 1.1  $\mu$ s at 1 V for a pixel area of 0.03 mm<sup>2</sup>. The fall time also decreases with decreasing pixel area (**Figure S12**, Supporting Information).

We find that an advantage of TFCA devices over TBAI devices is enhanced operating stability. We tracked the transient photocurrent response at a certain bias over time under the illumination of a pulsed laser source (see **Figure S13**, Supporting Information for the time traces). This allowed us to determine simultaneously light current and dark current from ON–OFF cycles. The light current of both TFCA and TBAI devices was relatively stable under bias, but the dark current was sensitive to bias. As shown in **Figure 4a,b**, the dark current of TBAI increased by 100 $\times$  within 16 h at 0.1 V, while the dark current of TFCA only increased by 2 $\times$ . We calculated the normalized response based on the following equation:

$$\text{Norm. response} = \frac{I_{\text{light}} - I_{\text{dark}}}{I_{\text{dark}}} \quad (1)$$

$I_{\text{light}}$  represents light current, and  $I_{\text{dark}}$  represents dark current. The normalized response of TFCA is 60 $\times$  more stable than TBAI at the same bias of 0.1 V (**Figure 4c**). When the bias is increased to 0.3 V (**Figure 4d,e**), the increase in dark current was dramatic in each class of devices: TBAI increased by 600 $\times$  and TFCA increased by 120 $\times$ . The normalized response dropped more significantly for both devices at 0.3 V than at 0.1 V, but TFCA was still more stable than TBAI (**Figure 4f**). We also tracked the changes in dark current at a few other bias voltages, and the increase in dark current was magnified with increasing bias (**Figure S14**, Supporting Information). The increase in dark current was not permanent. After removing the bias, the dark current recovered quickly to its original level (**Figure S15**, Supporting Information). Thus, mild bias ( $\leq 0.5$  V) does not cause permanent damage to the device, but only induces reversible changes.

Prior reports on the operating stability of CQD photodetectors that relied on metal oxides as ETLs were focused on photocurrent stability. CQD photodetectors that used sol–gel ZnO as ETL retained 71% of their initial photocurrent following 12 h of operation.<sup>[8]</sup> ZnO ETL produced by atomic layer deposition (ALD) improved the stability of CQD photodetectors significantly, their photocurrent remaining unchanged following 100 h of operation.<sup>[10]</sup> The present work instead looks at both the light current and dark current stability, including with bias.

We sought to understand the origin of different behaviors of dark current in the two classes of devices under bias, important to improving the operating stability of CQD photodetectors. Iodine ions, the binding species in TBAI exchanged-CQDs, are more likely to detach from the CQD surface than TFCA, due to the smaller binding energy of iodine (**Figure 1b**). The iodine

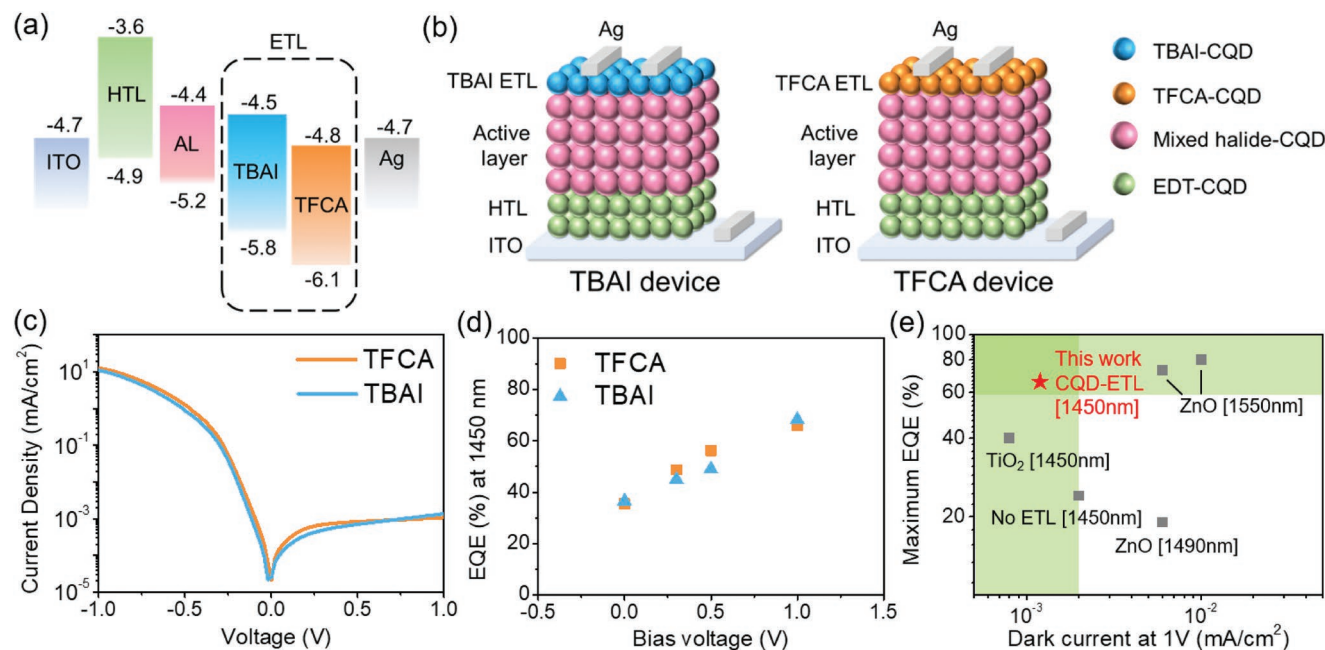


**Figure 2.** Energy band diagrams, device structures, and performance comparison. a) Band diagram of the full device determined using UPS combined with UV-vis absorption. AL stands for active layer. b) Schematic of device architecture using TFCA-CQDs or TBAI-CQDs as ETL. c) Current density–voltage ( $J$ – $V$ ) characteristics of TFCA and TBAI devices measured in the dark. d) EQE of TFCA and TBAI devices measured at different bias voltages. e) Comparison of device performance with reported SWIR photodetectors.<sup>[7–9,24,25]</sup> The different operating wavelengths and different ETLs (if used) are labeled next to each data point.

ions are prone to migrate under the external electric field, as often seen in perovskite solar cells or light-emitting diodes.<sup>[26–29]</sup> Iodine migration in perovskites can be detrimental to the device performance, often resulting in significant  $I$ – $V$  hysteresis and degrading device efficiency. For CQD solar cells, it was reported that the mobile ions of surface ligands can redistribute under external bias stress, leading to hysteresis and photo instability.<sup>[30]</sup> Previous work was only focused on the mobile protons in CQDs. For our CQD ETL system, we hypothesize that the migration of ligand anions prompted by the electric field is responsible for the instability of dark current.

We tested this hypothesis using impedance measurements, used in prior works to study ion migration.<sup>[31,32]</sup> Figure 5a,b compares the capacitance–frequency curves of TBAI and TFCA devices under different bias voltages. There is an increase in low-frequency capacitance with an increasing bias for TBAI;

whereas, for TFCA there is no such dependence of low-frequency capacitance on the bias. The change in high-frequency capacitance is negligible with an increasing bias for both devices. We also tracked the changes in capacitance at a fixed frequency when 0.3 V bias was continuously applied (Figure 5c,d). The capacitance at 10 Hz increased by 100× for TBAI, but remained stable for TFCA. The capacitance at 10<sup>5</sup> Hz remained unchanged for both devices. The impact of bias on low-frequency capacitance for TBAI and TFCA shows similar trends to the impact of bias on dark current in the two classes of devices.

The low-frequency capacitance is correlated to accumulated charges at the interfaces, mostly of ionic character in the dark.<sup>[31,32]</sup> The high-frequency capacitance corresponds to the geometrical capacitance, which is determined by the dielectric constants and thicknesses of layers. Based on these results, we offer two possible scenarios (Figure 5e): when a small bias is

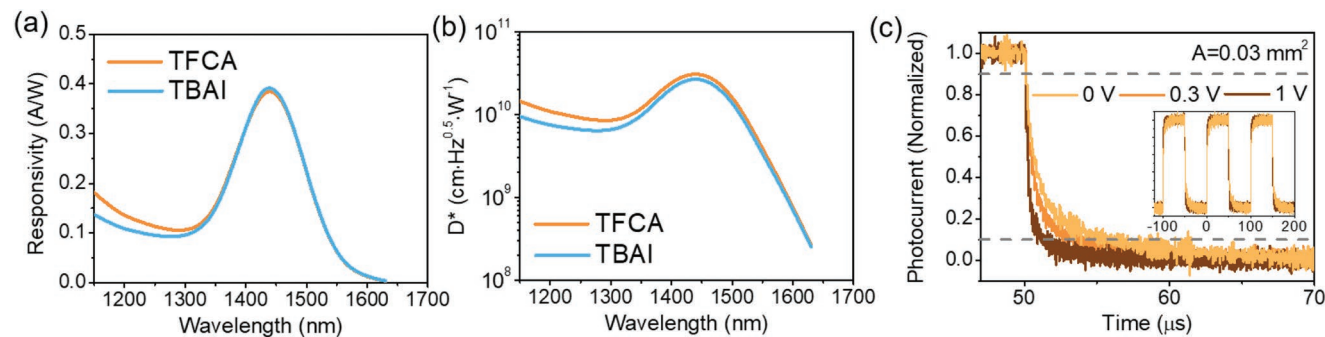


**Figure 3.** Photodetector characterization. a) Responsivities and b) detectivities of TFCA and TBAI devices measured at 0 V. c) Transient photocurrent responses of TFCA devices with a pixel area of 0.03 mm<sup>2</sup> at different bias voltages. Inset shows three ON–OFF cycles.

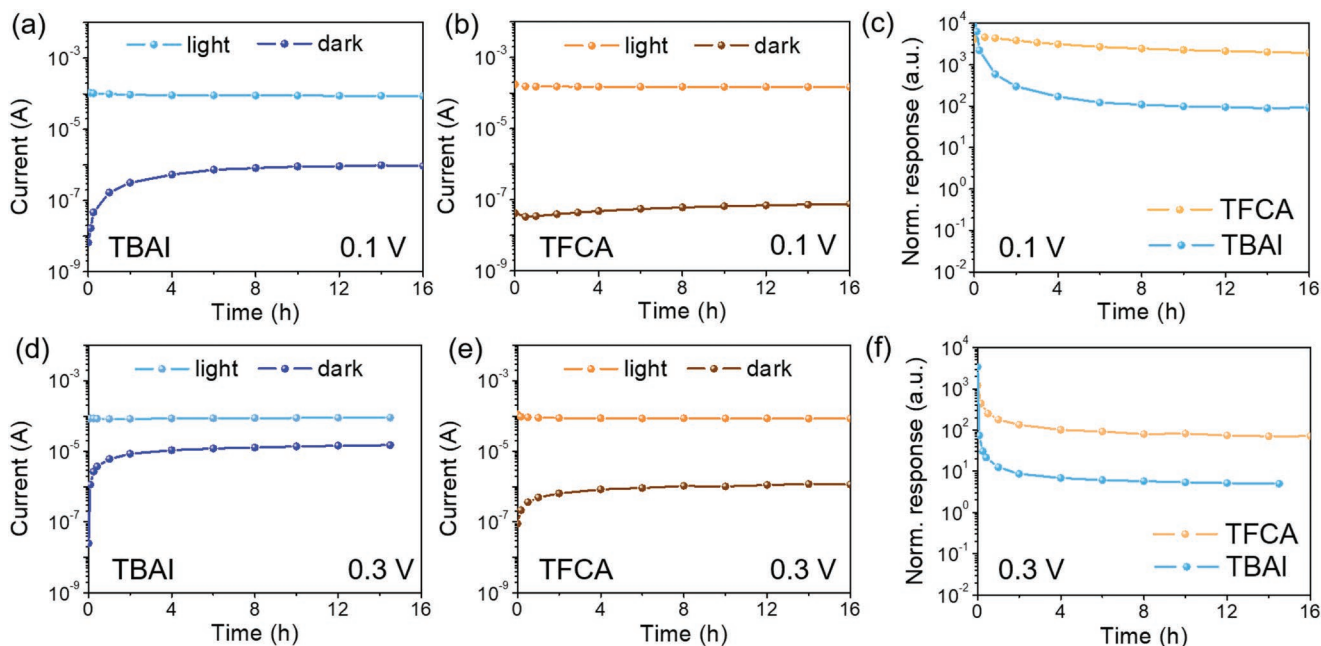


**Figure 4.** Operating stability comparison under bias. a,b) Light current and dark current of TBAI devices (a) and TFCA devices (b) over time at a constant bias of 0.1 V. c) Normalized response comparison of both devices over time at 0.1 V. d,e) Light current and dark current of TBAI devices (d) and TFCA devices (e) over time at 0.3 V. f) Normalized response comparison of both devices over time at 0.3 V.

applied to the device for a short time, there is a small amount of ligand anions accumulated at the ETL/Ag interface, correspondingly  $I^-$  for TBAI, and  $TFCA^-$  for TFCA; when the bias or the duration of bias is increased, the amount of accumulated  $I^-$  at the interface increases significantly for TBAI devices, but the amount of accumulated  $TFCA^-$  does not change for TFCA devices.

It is crucial to suppress the dark current in photodetectors, as it serves as the main source of noise, and would negatively impact the detectivity. Surface defects are responsible for the surface leakage current, an important component of dark current.<sup>[33,34]</sup> In TBAI devices, the weakly bound ligands cannot provide enough passivation for ETL CQDs, and the mobile ions on the CQD surface tend to redistribute under bias. This could lead to an increasing population of defects inside the ETL and at the interfaces, and consequently an increasing dark current in photodetectors. By using a strongly bound TFCA ligand, we improve the passivation of CQDs in the ETL, reduce the impact of bias on ion migration, and thus stabilize the dark current in TFCA devices.

The stability improvement of TFCA devices over TBAI devices is more prominent in dark current than light current. The light current is dominated by photogenerated charge carriers. The contribution of ion migration to light current is small (on the order of  $1 \times 10^{-3}$  to  $1 \times 10^{-2}$  mA cm<sup>-2</sup>), compared to the contribution of photogenerated carriers to light current (on the order of 1–10 mA cm<sup>-2</sup>). In contrast, the dark current is on the order of  $1 \times 10^{-3}$  mA cm<sup>-2</sup>, so the impact of ion migration on dark current is more obvious.

### 3. Conclusions

This work develops CQD-based ETLs as a replacement for the conventional metal-oxide-based ETLs used in CQD

photodetectors. CQDs of different bandgaps and ligand passivation are combined in a single photodetector to achieve different key roles as the active layer and the transport layers. With the improved band alignment at the active layer/ETL interface, we demonstrate CQD photodetectors operating at 1450 nm, with a low dark current of  $\approx 1 \times 10^{-3}$  mA cm<sup>-2</sup> and a high EQE of  $\approx 66\%$  at 1 V, surpassing the prior works that used metal oxide as ETLs. We find that weakly bound inorganic ligands can lead to ion migration inside the ETL, and consequently performance degradation in CQD photodetectors under bias. Instead, a strongly bound organic ligand TFCA provides better passivation of ETL CQDs, suppresses the bias-induced ion migration, and greatly improves the operating stability of CQD photodetectors. The work introduces new materials set, as well as new durability science principles, into ETL materials for stable SWIR CQD photodetectors.

### 4. Experimental Section

**Synthesis of PbS CQDs:** Two different sizes of oleic-acid-capped PbS CQDs were used in this work, including the larger CQDs (with an exciton peak at 1450 nm) for the active layer and the smaller CQDs (with an exciton peak at 950 nm) for both the ETL and the HTL. Both sizes of CQDs were synthesized using a published method<sup>[35]</sup> with modified amount of bis(trimethylsilyl) sulfide precursor and injection temperature for size tuning.

**EDT Ligand Exchange:** A reported layer-by-layer ligand exchange was used to fabricate EDT-CQD films under ambient conditions.<sup>[22]</sup> Oleic-acid-capped PbS CQDs with an excitonic peak at 950 nm were used for the exchange. 47  $\mu$ L of CQDs were spin-coated on top of ITO substrates at 2500 RPM for 10 s. Then, the layer was soaked in 0.01% EDT solution in a solvent mixture of acetonitrile:ethyl acetate (volume ratio 1:3) for 30 s. The sample was spun again with the same parameters, and the acetonitrile:ethyl acetate solvent mixture without EDT was used

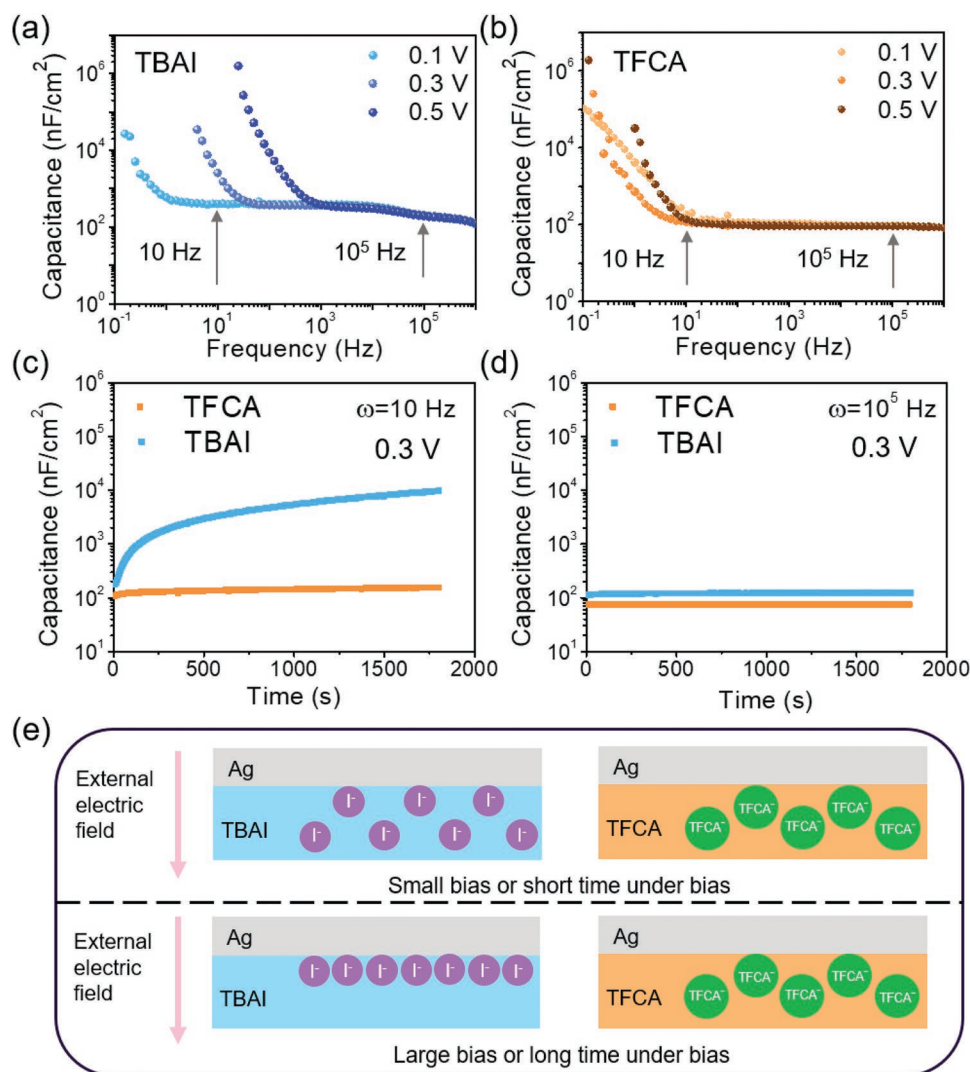


**Figure 5.** Mechanism of stability improvement. a,b) Capacitance–frequency plots of TBAI devices (a) and TFCA devices (b) measured at different bias voltages. c,d) Capacitance–time plots of TBAI and TFCA devices measured at different frequencies when 0.3 V bias was applied: c) 10 Hz and d) 10<sup>5</sup> Hz. e) Schematic of the different anion behaviors in TBAI and TFCA ETLs in different scenarios: a small bias or short time under bias, compared to large bias or long time under bias.

to wash the sample three times. The whole process was repeated twice to deposit two layers of EDT-CQDs.

**Mixed Halide Ligand Exchange:** The solution-phase mixed halide ligand exchange was conducted under ambient conditions following a published method.<sup>[22]</sup> Oleic-acid-capped PbS CQDs with an excitonic peak at 1450 nm were used for the exchange. The halide exchange solution was prepared by dissolving 0.231 g of PbI<sub>2</sub>, 0.147 g of PbBr<sub>2</sub>, 0.139 g of PbCl<sub>2</sub>, and 0.036 g of NaAc in 10 mL DMF. Then, 20 mL of octane and 1.4 mL of CQDs were added to the exchange solution in a centrifuge tube. The ligand exchange was initiated by vortexing the above mixture for 4 min. After the CQDs have transferred to the bottom DMF phase, the washing step was initiated by removing the top octane phase. This octane washing step was repeated three times. Each time 20 mL of octane was added to the centrifuge tube, and the tube was vortexed for 30 s. After the washing steps, the octane was removed and 2.5 mL of toluene was added dropwise to the mixed halide passivated CQDs. The solution was centrifuged and the supernatant was discarded. The CQDs were dried under vacuum for 7 min before redispersion. The CQDs were dispersed in a solvent mixture of DMF and butylamine (volume ratio 1:4) at a concentration of 300 mg mL<sup>-1</sup>.

**TFCA Ligand Exchange:** The solution-phase TFCA ligand exchange was conducted in a nitrogen-filled glovebox using a slightly modified method from the literature.<sup>[19]</sup> Oleic-acid-capped PbS CQDs with an excitonic peak at 950 nm were used for the exchange. The TFCA ligand solution was prepared by dissolving 0.064 g of TFCA in 2 mL of acetone, and filtered before use. Inside a nitrogen-filled glovebox, 1.5 mL of TFCA ligand solution was added dropwise to 0.5 mL of CQDs (at a concentration of 50 mg mL<sup>-1</sup> in toluene) with continuous stirring. The mixed solution was stirred for 1 h to ensure complete ligand exchange. After the exchange, 4 mL of octane was added to the TFCA-exchanged CQDs, followed by centrifuging. The supernatant was discarded and the precipitate was dispersed in 0.5 mL methyl acetate. Then, the CQDs were washed three times, each time with 1 mL octane. After the washing steps, the supernatant was removed, and the CQDs were dried under vacuum for 60 s. The dried CQDs were dispersed in methyl acetate.

**TBAI Ligand Exchange:** A reported layer-by-layer ligand exchange<sup>[14]</sup> was used to form TBAI-exchanged CQD films. Oleic-acid-capped PbS CQDs with an excitonic peak at 950 nm were used for the exchange. 47 μL of CQDs were spin-coated on top of ITO substrates at 2500 RPM for 10 s. Then, the layer was soaked in TBAI solution (10 mg mL<sup>-1</sup> in

ethanol) for 30 s. The sample was spun again with the same parameters, and acetonitrile was used to wash the sample twice. The whole process was repeated twice to deposit two layers of TBAI-CQDs.

**Device Fabrication:** Pre-patterned indium tin oxide (ITO) glass substrates were cleaned with DI water, acetone, and isopropyl alcohol respectively, and dried before use. The substrates were O<sub>3</sub>-plasma treated for 10 min to improve the adhesion of the following layers. Two layers of EDT-CQDs were deposited as the HTL, as described in EDT ligand exchange. The films were left in dry air for 24 h. For the active layer deposition, 47  $\mu$ L of mixed halide exchanged CQD ink (produced by mixed halide ligand exchange) were spin-coated dynamically on top of the HTL at 1000 RPM for 40 s under a nitrogen flow. The deposited films were annealed at 70 °C in a nitrogen-filled glovebox for 15 min. For the ETL, either two layers of TBAI-exchanged CQDs or one layer of TFCA-exchanged CQDs were deposited on top of the active layer (as described in TBAI ligand exchange or TFCA ligand exchange) inside a nitrogen-filled glovebox. For TFCA layer of 10 nm thickness, 47  $\mu$ L of TFCA-CQD ink at a concentration of 4 mg mL<sup>-1</sup> was spin-coated dynamically at 1500 to 2000 RPM for 50 s. After ETL deposition, the films were left in a nitrogen-filled glovebox for 24 h. Finally, a 140 nm layer of silver was deposited as the top electrode using thermal evaporation.

**Materials Characterization:** Scanning transmission electron microscopy and high-resolution TEM images of the CQDs samples were acquired with HF-3300 transmission electron microscope. Samples were prepared by drop-casting diluted dispersion of CQDs. FTIR spectra were obtained in the attenuated total reflectance mode using an FTIR spectrometer (Thermo Scientific iS50) in the spectral range of 4600–50 cm<sup>-1</sup>. Samples were prepared on glass substrates. XPS was measured using a Thermo Scientific K-Alpha system for CQDs deposited on ITO substrates. UPS measurement was carried out using an ESCALAB 250Xi system. A helium lamp (He-I  $\alpha$ ,  $h\nu = 21.22$  eV) was used as the radiation source, and the samples were kept under -5 V bias during the measurement. The samples were prepared on ITO substrates. SCLC measurement was conducted by measuring the dark  $I$ - $V$  of an electron-only device with ITO/ZnO/ $n$ -type CQD/LiF/Ag structure.

For transient absorption (TA) measurements, a regeneratively amplified Yb:KGW laser at a 5 kHz repetition rate (Light Conversion, Pharos) was used to generate femtosecond laser pulses. The samples were photoexcited with 130  $\mu$ W 560 nm pump pulse. The time delay between pump and probe was adjusted by changing the path length of the probe (time resolution  $\approx$ 350 fs). The probe pulse was then collected by a CCD after dispersion by a grating spectrograph (Ultrafast). Multiple excitation powers were checked to make sure that the excitation was within the linear regime to avoid the multi-carrier process and strong Auger recombination.

**Device Characterization:** Current-voltage measurements were taken using a Keithley 2400 source meter in the dark. The  $I$ - $V$  curves were scanned from -1 V to +1 V at 0.02 V interval steps without delay time between voltage steps.

The EQEs of devices were measured using a homemade high dynamic range EQE system. The calibration procedure was conducted before each set of measurements using a standard calibrated Si/Ge reference detector (BD005, Newport). EQE spectra were taken by subjecting the devices to chopped (30–150 Hz) monochromatic illumination (Xe lamp passing through a monochromator and appropriate cutoff filters). The response of the devices was measured with a Stanford Research SR570 pre-amplifier feeding into a Stanford Research SR830 lock-in amplifier.

The temporal response of the photodetectors was recorded using a 1-GHz oscilloscope (DSO8104A Infinium, Agilent). A 1310 nm diode laser (Thorlabs ML725B8F) modulated at a frequency of 10 kHz using a function generator (Agilent 33220A) was used to illuminate the pixels. Photodetector signal was pre-amplified (10<sup>3</sup> V A<sup>-1</sup>) using a pre-amplifier (Femto DHPA-100). The photodetector was biased through the pre-amplifier when applicable.

Noise spectra were measured using a signal analyzer (N9010A, Agilent) combined with a low noise pre-amplifier. Noise measurements were carried out in the dark at room temperature for the pixels with 0.1 cm<sup>2</sup> area. The noise current was calculated using the noise signal measured at 10 kHz and amplification of 10<sup>6</sup> V A<sup>-1</sup> from the preamplifier.

The detectivity was calculated based on noise current, responsivity, set bandwidth of 1 Hz, and active area.<sup>[8]</sup>

The impedance spectrum was measured using a potentiostat electrochemical workstation (AUT50690, PGSTAT204, The Netherlands) at different bias voltages. The frequency ranged from 1 MHz to 0.1 Hz.

The operational stability of photodetectors was assessed using an 825 nm diode laser controlled by a function generator (Tektronix AFG 31000) which produces pulses with a frequency of 2.5 kHz. The transient response of the devices (pixel size of 0.1 cm<sup>2</sup>) under different bias voltages was recorded on the 8-GHz oscilloscope (Tektronix 6 series MSO64B). The dark current and the light current were calculated based on the minimum and the maximum response voltage using an amplification of 10<sup>6</sup> V A<sup>-1</sup>. The devices were encapsulated in a nitrogen environment prior to the stability tests.

**DFT Simulation:** First-principles calculations based on DFT were carried out using the Vienna Ab initio Simulation Package (VASP).<sup>[36]</sup> The generalized gradient approximation of Perdew–Burke–Ernzerhof functional was used as the exchange-correlation functional.<sup>[37]</sup> The DFT-D3 method was included for the van der Waals (vdW) correction.<sup>[38]</sup> The plane-wave cutoff energy of 400 eV was used. The energy and force convergence criteria were set to 10<sup>-5</sup> eV and 0.02 eV Å<sup>-1</sup>, respectively. Different adsorption sites of ligands on PbS surfaces were considered, including Pb-top, S-top, and hollow sites, and it was found that hollow site was the most stable adsorption configuration.

**Statistical Analysis:** The data were used without any transformation with the exception of Figure 3c. The transient photocurrent response in Figure 3c was normalized to the maximum photocurrent. For the device performance in Figure 2c,d, at least 3 samples were measured, and a representative sample was used for plotting.

## Supporting Information

Supporting Information is available from the Wiley Online Library or from the author.

## Acknowledgements

Y.Z. and M.V. contributed equally to this work. This work was supported by the Natural Sciences and Engineering Research Council of Canada (RPGIN-2017-06477) and the Canada Research Chairs (CRC-2017-00318). The authors would like to thank L. Levina, E. Palmiano, R. Wolowiec, and D. Kopolovic for their technical assistance.

## Conflict of Interest

The authors declare no conflict of interest.

## Data Availability Statement

The data that support the findings of this study are available from the corresponding author upon reasonable request.

## Keywords

colloidal quantum dots, electron-transport layer, ion migration, photodetectors, short-wavelength infrared

Received: July 28, 2022  
Revised: September 4, 2022  
Published online:

- [1] M. P. Hansen, D. S. Malchow, *Proc. SPIE* **2008**, 6939, 693901.
- [2] F. Holzwarth, U. Eichhorn, *Sens. Actuators, A* **1993**, 37–38, 121.
- [3] L. Tharmakularajah, J. Döring, K.-L. Krieger, *J. Sens. Sens. Syst.* **2020**, 9, 133.
- [4] F. P. García de Arquer, D. V. Talapin, V. I. Klimov, Y. Arakawa, M. Bayer, E. H. Sargent, *Science* **2021**, 373, 640.
- [5] F. P. García De Arquer, A. Armin, P. Meredith, E. H. Sargent, *Nat. Rev. Mater.* **2017**, 2, 16100.
- [6] R. Sliz, M. Lejay, J. Z. Fan, M. J. Choi, S. Kinge, S. Hoogland, T. Fabritius, F. P. García De Arquer, E. H. Sargent, *ACS Nano* **2019**, 13, 11988.
- [7] V. Pejovic, J. Lee, E. Georgitzikis, Y. Li, J. H. Kim, I. Lieberman, P. E. Malinowski, P. Heremans, D. Cheyns, *IEEE Electron Device Lett.* **2021**, 42, 1196.
- [8] M. Vafaie, J. Z. Fan, A. Morteza Najarian, O. Ouellette, L. K. Sagar, K. Bertens, B. Sun, F. P. García de Arquer, E. H. Sargent, *Matter* **2021**, 4, 1042.
- [9] M. Biondi, M. J. Choi, Z. Wang, M. Wei, S. Lee, H. Choubisa, L. K. Sagar, B. Sun, S. W. Baek, B. Chen, P. Todorović, A. M. Najarian, A. Sedighian Rasouli, D. H. Nam, M. Vafaie, Y. C. Li, K. Bertens, S. Hoogland, O. Voznyy, F. P. García de Arquer, E. H. Sargent, *Adv. Mater.* **2021**, 33, 2101056.
- [10] D. H. Parmar, J. M. Pina, T. Zhu, M. Vafaie, O. Atan, M. Biondi, A. M. Najarian, S. Hoogland, E. H. Sargent, *Adv. Mater.* **2022**, 34, 2200321.
- [11] S. Lee, M. J. Choi, G. Sharma, M. Biondi, B. Chen, S. W. Baek, A. M. Najarian, M. Vafaie, J. Wicks, L. K. Sagar, S. Hoogland, F. P. García de Arquer, O. Voznyy, E. H. Sargent, *Nat. Commun.* **2020**, 11, 4814.
- [12] M. Biondi, M. J. Choi, O. Ouellette, S. W. Baek, P. Todorović, B. Sun, S. Lee, M. Wei, P. Li, A. R. Kirmani, L. K. Sagar, L. J. Richter, S. Hoogland, Z. H. Lu, F. P. García de Arquer, E. H. Sargent, *Adv. Mater.* **2020**, 32, 1906199.
- [13] Z. Yang, O. Voznyy, M. Liu, M. Yuan, A. H. Ip, O. S. Ahmed, L. Levina, S. Kinge, S. Hoogland, E. H. Sargent, *ACS Nano* **2015**, 9, 12327.
- [14] Z. Ning, O. Voznyy, J. Pan, S. Hoogland, V. Adinolfi, J. Xu, M. Li, A. R. Kirmani, J. P. Sun, J. Minor, K. W. Kemp, H. Dong, L. Rollny, A. Labelle, G. Carey, B. Sutherland, I. Hill, A. Amassian, H. Liu, J. Tang, O. M. Bakr, E. H. Sargent, *Nat. Mater.* **2014**, 13, 822.
- [15] X. Lan, O. Voznyy, A. Kiani, F. P. García De Arquer, A. S. Abbas, G. H. Kim, M. Liu, Z. Yang, G. Walters, J. Xu, M. Yuan, Z. Ning, F. Fan, P. Kanjanaboos, I. Kramer, D. Zhitomirsky, P. Lee, A. Perelgut, S. Hoogland, E. H. Sargent, *Adv. Mater.* **2016**, 28, 299.
- [16] Q. Xu, L. Meng, K. Sinha, F. I. Chowdhury, J. Hu, X. Wang, *ACS Photonics* **2020**, 7, 1297.
- [17] J. M. Pina, M. Vafaie, D. H. Parmar, O. Atan, P. Xia, Y. Zhang, A. M. Najarian, F. P. Garcia, S. Hoogland, E. H. Sargent, *Nano Lett.* **2022**, 22, 6802.
- [18] G. W. Hwang, D. Kim, J. M. Cordero, M. W. B. Wilson, C. H. M. Chuang, J. C. Grossman, M. G. Bawendi, *Adv. Mater.* **2015**, 27, 4481.
- [19] D. M. Kroupa, M. Vörös, N. P. Brawand, B. W. McNichols, E. M. Miller, J. Gu, A. J. Nozik, A. Sellinger, G. Galli, M. C. Beard, *Nat. Commun.* **2017**, 8, 15257.
- [20] G. Shi, H. Wang, Y. Zhang, C. Cheng, T. Zhai, B. Chen, X. Liu, R. Jono, X. Mao, Y. Liu, X. Zhang, X. Ling, Y. Zhang, X. Meng, Y. Chen, S. Duhm, L. Zhang, T. Li, L. Wang, S. Xiong, T. Sagawa, T. Kubo, H. Segawa, Q. Shen, Z. Liu, W. Ma, *Nat. Commun.* **2021**, 12, 4381.
- [21] Y. Kim, F. Che, J. W. Jo, J. Choi, F. P. García de Arquer, O. Voznyy, B. Sun, J. Kim, M. J. Choi, R. Quintero-Bermudez, F. Fan, C. S. Tan, E. Bladt, G. Walters, A. H. Proppe, C. Zou, H. Yuan, S. Bals, J. Hofkens, M. B. J. Roeflaers, S. Hoogland, E. H. Sargent, *Adv. Mater.* **2019**, 31, 1805580.
- [22] J. Z. Fan, N. T. Andersen, M. Biondi, P. Todorović, B. Sun, O. Ouellette, J. Abed, L. K. Sagar, M. J. Choi, S. Hoogland, F. P. García de Arquer, E. H. Sargent, *Adv. Mater.* **2019**, 31, 1904304.
- [23] P. R. Brown, D. Kim, R. R. Lunt, N. Zhao, M. G. Bawendi, J. C. Grossman, V. Bulovic, *ACS Nano* **2014**, 8, 5863.
- [24] J. P. Clifford, G. Konstantatos, K. W. Johnston, S. Hoogland, L. Levina, E. H. Sargent, *Nat. Nanotechnol.* **2009**, 4, 40.
- [25] X. Xiao, K. Xu, M. Yin, Y. Qiu, W. Zhou, L. Zheng, X. Cheng, Y. Yu, Z. Ning, *Appl. Phys. Lett.* **2020**, 116, 101102.
- [26] C. Eames, J. M. Frost, P. R. F. Barnes, B. C. O'Regan, A. Walsh, M. S. Islam, *Nat. Commun.* **2015**, 6, 7497.
- [27] D. Di Girolamo, N. Phung, F. U. Kosasih, F. Di Giacomo, F. Matteocci, J. A. Smith, M. A. Flatken, H. Köbler, S. H. Turren Cruz, A. Di Mattoni, L. Cinà, B. Rech, A. Latini, G. Divitini, C. Ducati, A. Di Carlo, D. Dini, A. Abate, *Adv. Energy Mater.* **2020**, 10, 2000310.
- [28] H. Wang, Z. Chen, J. Hu, H. Yu, C. Kuang, J. Qin, X. Liu, Y. Lu, M. Fahlman, L. Hou, X. K. Liu, F. Gao, *Adv. Funct. Mater.* **2021**, 31, 2007596.
- [29] N. Li, Y. Jia, Y. Guo, N. Zhao, *Adv. Mater.* **2022**, 34, 2108102.
- [30] J. H. Song, X. D. Mai, S. Jeong, Y. H. Kim, *J. Phys. Chem. Lett.* **2017**, 8, 5259.
- [31] O. Almora, I. Zarazua, E. Mas-Marza, I. Mora-Sero, J. Bisquert, G. Garcia-Belmonte, *J. Phys. Chem. Lett.* **2015**, 6, 1645.
- [32] I. Zarazua, G. Han, P. P. Boix, S. Mhaisalkar, F. Fabregat-Santiago, I. Mora-Seró, J. Bisquert, G. Garcia-Belmonte, *J. Phys. Chem. Lett.* **2016**, 7, 5105.
- [33] G. R. Savich, J. R. Pedrazzani, D. E. Sidor, S. Maimon, G. W. Wicks, *Appl. Phys. Lett.* **2011**, 99, 2009.
- [34] Z. Jiang, W. Hu, Y. Liu, W. Zhang, C. Mo, G. You, L. Wang, M. R. M. Atalla, Y. Zhang, J. Liu, K. K. Kurhade, J. Xu, *Appl. Phys. Lett.* **2015**, 107, 09115.
- [35] M. A. Hines, G. D. Scholes, *Adv. Mater.* **2003**, 15, 1844.
- [36] G. Kresse, J. Furthmüller, *Phys. Rev. B* **1996**, 54, 11169.
- [37] J. P. Perdew, K. Burke, M. Ernzerhof, *Phys. Rev. Lett.* **1996**, 77, 3865.
- [38] K. Lee, É. D. Murray, L. Kong, B. I. Lundqvist, D. C. Langreth, *Phys. Rev. B* **2010**, 82, 81101.